Effect of microstructural defects on passive layer properties of interstitial free (IF) ferritic steels in alkaline environment

A. Yilmaz [a,b,c], K. Traka [a,b,d], S. Pletincx [e], T. Hauffman [e], J. Sietsma [a], Y. Gonzalez-Garcia [a,*]

[a] Delft University of Technology, Department of Materials Science and Engineering, Mekelweg 2, 2628 CD, Delft, the Netherlands
[b] Materials innovation institute (M2i), Elektronicaweg 25, 2628 XG, Delft, the Netherlands
[c] Netherlands Organisation for Scientific Research, NWO, Van Vollenhovenlaan 659-661, 3527 JP, Utrecht, the Netherlands
[d] Max-Planck-Institut für Eisenforschung GmbH, Max-Planck-Straße 1, 40237, Düsseldorf, Germany
[e] Department of Materials and Chemistry, Research Group Electrochemical and Surface Engineering (SURF), Vrije Universiteit Brussel, Pleinlaan 2, B-1050, Brussels, Belgium

ARTICLE INFO

ABSTRACT

The role of microstructural defects (dislocation density and grain boundary areas) on the passive film properties formed on cold- and hot-rolled interstitial free (IF) steels is investigated in 0.1 M NaOH solution. Electron backscattered diffraction (EBSD) shows higher microstructural defect density on cold-rolled samples. Potentiodynamic polarization (PDP) and electrochemical impedance spectroscopy (EIS) results exhibit the lower barrier properties of passive films with the increase in microstructural defects. This is attributed to the increase in donor density measured with Mott-Schottky analysis and the lower relative quantity of protective γ-Fe_2O_3 in passive films (composed of Fe_3O_4,γ-Fe_2O_3 and FeO(OH)) with the increase in microstructural defect density.

1. Introduction

Cold working is commonly applied on steels in many industries, varying from automotive to oil and gas in order to increase the strength and hardness of materials during fabrication procedures [1]. The improved mechanical properties mainly stem from the higher defect density (dislocation and grain boundary density) achieved after cold working. A significant number of studies has widely investigated the relationship between defect density and mechanical properties [2–4]. However, the understanding of the relationship between defect density and passivity is still to be improved. During the processes to manipulate the defect density, other changes in the microstructure of the substrate material also occur [5–7]. These other microstructural changes, e.g. segregation of alloying elements, phase transformation, the formation of inclusions, affect passive layer properties with different defect density.

The effect of these microstructural features might interfere with or dominate the impact of defect density on the passive layer properties. This leads to contradictory reports on the effect of dislocation density on the passivity behaviour in the existing literature. Both improvement and deterioration in the barrier properties of the passive film with an increase in defect density are reported [8–12]. Jinlong and Hongyun [8] studied the effect of pre-deformation, resulting in the rise in both dislocation density and the volume fraction of α'-martensite, on passive layer properties of AISI 304 stainless steel. They reported the deterioration of passive layer barrier properties with an increase in pre-deformation. Yamamoto et al. [11] investigated the role of different degrees of cold working on the passivation behaviour of pure iron. They observed first a decrease and then an enhancement in the barrier properties of the passive film with increasing cold working degrees, leading to an increase in the defect density. Wang and Li [12] compared the electrochemical behaviour of nanocrystalline and as received 304 stainless steels. The nanocrystalline material was obtained with sandblasting, leading to a significant increase in dislocation density and decrease grain size. They observed better passive layer properties in nanocrystalline material after sandblasting. These existing studies show that it is not straightforward to establish a relationship between defect density and passive layer properties due to the changes in other microstructure features, occurring during the processes used to change the defect density. Considering the contradictory results presented in the literature, it is only possible to understand the sole role of defect density on the passive layer properties by designing and controlling the microstructure.

Furthermore, the majority of abovementioned studies focused on the passivity behaviour of stainless steels [8–10,12]. Very few studies

---

investigated the role of microstructural defect density on passive layer properties of low alloyed steels [11]. The existing literature explained the changes in electrochemical properties of passive films are associated to the variations in the donor/acceptor density in the passive films due to the presence of substrate microstructural defects [8–11]. Yet, very little attention has been given to the alterations in the chemical composition and thickness of the passive layer with variations in microstructural defect density, that change the barrier properties of passive films.

The goal of this work is to deepen the understanding of the relation between microstructural defect density and passive layer behaviour of high-strength steels. For this purpose, controlled alloys of hot- and cold-rolled interstitial free (IF) steels were employed to minimize the changes in microstructural features other than the defect density. The effect of microstructural defect density on the barrier properties of passive films was investigated with potentiodynamic polarization (PDP) and electrochemical impedance spectroscopy (EIS) in 0.1 M NaOH. The donor density of passive films was characterized by Mott-Schottky analysis. The chemical composition and thickness of the passive films were evaluated by X-ray photoelectron spectroscopy (XPS) and ellipsometry, respectively. Scanning Kelvin probe (SKP) measurements were conducted to determine the effect of microstructural defect density on surface reactivity. The experimental results form the basis for a discussion on the role of defect density on the properties of the passive film.

2. Experimental

2.1. Material

Hot and cold rolled interstitial-free (IF) ferritic steels (provided by Tata Steel, the Netherlands) were investigated. The chemical composition of IF steel employed is given in Table 1. The thickness reduction at the last pass of hot-rolling was approximately 85 %, and the cold-rolling reduction was approximately 78 %. Hot rolled and cold rolled samples are indicated as low defect density (LD) and high defect density (HD) samples, respectively. The thickness of hot- and cold-rolled samples were 3.4 and 0.76 mm, respectively. Both samples were laser-cut to the dimension of 10 × 5 mm.

2.2. Microstructure characterization

Electron backscattered diffraction (EBSD) analysis was employed to characterize the microstructures, by obtaining information about crystallographic phases and orientation, grain boundary area fraction and dislocation density. The calculation of Geometrically Necessary Dislocations (GND) density was performed with OIM v7.3 software using the function described in [13]. The method approximates the dislocation content ρ_{GND} by its relation to the dislocation tensor (known as Nye's tensor [14]) which is calculated as the tensorial summation of the lattice curvature (i.e. orientation's *curl*) and the elastic strain tensor's divergence, as it was initially proposed by Nye in [14]. To prepare the samples for electron backscattered diffraction (EBSD) analysis, the samples were ground with SiC papers of 80–4000 grit. Afterwards, the samples were polished with a diamond particle slurry with particle sizes of 3 and 1 μm (Struers DiaDuo-2), respectively. The samples were finally polished with a standard colloidal silica suspension with a 0.04 μm particle size. Then, the samples were cleaned in an ultrasonic bath with ethanol for 10 min and dried with compressed air. The high-resolution EBSD

measurements were conducted with a JEOL JSM 6500 F FEG-SEM microscope with an EDAX/TSL detector. A working distance of 17 mm and the step size of 0.5 μm were used for all EBSD measurements. The post-processing of the EBSD data was conducted both in TSL-OIM version 7.3 and in Matlab with the use software tool provided by MTEX [15].

2.3. Scanning Kelvin probe measurements

Scanning Kelvin probe measurements were conducted to investigate the relationship between microstructural defect density and surface reactivity. The samples for Scanning Kelvin probe (SKP) measurements were prepared as follows. The samples were mechanically ground with SiC grinding papers, from 80–4000 grit. Following grinding, the samples were polished with alcohol-based, high-performance diamond slurry, having particles size of 3 μm (Struers DP-Suspension A), and polishing cloth (Struers DP-Mol). Finally, the samples were polished with a 1 μm alcohol based-high performance diamond slurry (Struers DP-Suspension A) and polishing cloth (Struers DP-Nap) until obtaining mirror-like surface finishing. The samples were cleaned in an ultrasonic bath in ethanol for 10 min and dried with compressed air before the SKP measurements. A height-regulated scanning Kelvin probe (SKP5050) from KM Soft Control was employed to conduct potential measurements right after the sample preparation. The SKP probe consisted of an SAE 304 stainless steel tip with a diameter of approximately 550 μm. Before the measurements, the probe was calibrated against $Cu/CuSO_4$ reference. The experiments with the IF-steel samples were conducted on freshly polished samples at a controlled relative humidity of ambient air, −43 % and room temperature (23 °C). The potential was measured as a function of time. Point measurements were repeated three times for each sample to ensure reproducibility of the results.

2.4. Electrochemical measurements

Electrochemical measurements (potentiodynamic polarization, electrochemical impedance spectroscopy) were employed to investigate the effect of microstructural density on the electrochemical properties of passive film formed on both LD and HD samples.

Type-K chromel-alumel thermocouple wire was spot welded on the bottom of the samples to ensure a good connection of the working electrode to the electrochemical cell. Prior to electrochemical measurements, the samples were embedded in an epoxy resin (Struers ClaroCit). The resin was cured for 1 h under 2 bar pressure. Subsequently, the samples were mechanically ground and polished by the same procedure for samples preparation for SKP measurements. Afterwards, the samples were cleaned in an ultrasonic bath in ethanol for 10 min and dried with compressed air. To prevent crevice corrosion, the gap between the resin and the sample was masked by a thin layer of sealing lacquer (Electrolube Bloc Lube Red).

The electrolyte used for the electrochemical measurements was an aerated 0.1 M NaOH solution with a pH of 12.7. The solution was prepared with distilled water at room temperature. A conventional three-electrode electrochemical cell was used for the electrochemical measurements. The setup is composed of the sample as the working electrode, a graphite rod as counter electrode and a Ag/AgCl (Sat. KCl) reference electrode. A Biologic SP 300 potentiostat was used. The potentials were measured versus Ag/AgCl (Sat. KCl). The electrochemical tests were conducted three times to verify the reproducibility of the results.

Before conducting the electrochemical tests, the open circuit potential (OCP) was measured for 1800 s at which steady-state is achieved. For potentiodynamic polarization, a potential range between -0.25 V to 1.25 V (vs OCP) and a scan rate of 0.167 mV/s were chosen. Before EIS measurements, potentiostatic polarization was conducted at 0.2 V (vs. Ag/AgCl) for 3 h at which steady-state was observed for both samples to form the passive layer. Then, EIS measurements were obtained between

Table 1
Chemical composition of the IF- ferritic steel specimens.

	Fe	C	Mn	Al	N	Ti	S	Cr
wt%	99.78	0.002	0.095	0.05	0.002	0.045	0.006	0.02

30 kHz and 10 mHz with an A.C. signal, having an amplitude of 10 mV peak to peak. Zview software (v3.5) was employed for analyzing the EIS data.

Capacitance measurements (Mott-Schottky analysis) were conducted to correlate the microstructural defect density with the electronic properties of the passive film after forming the passive layer with potentiostatic polarization at 0.2 V (vs. Ag/AgCl) for 3 h. Capacitance measurements (Mott-Schottky analysis) were performed at the frequency of 1 kHz with an amplitude of 10 mV peak to peak for the AC signal. The potential sweeps were conducted from 0.6 V to −1 V with the potential step size of 50 mV. To analyze data from polarization and capacitance measurements, ECLab software (v11.33) was used.

2.5. Passive layer analysis

X-ray photoelectron spectroscopy (XPS) measurements were conducted to analyze the chemical composition and relative fractions of different (hydr)oxide layers in the passive layer, depending on the substrate defect density. Before XPS measurements, the passive layer was formed by potentiostatic polarization at 0.2 V (vs. Ag/AgCl) for 3 h in 0.1 M NaOH solution. Subsequently, the samples were rinsed with ethanol and dried with compressed air. A PHI5000 Versaprobe II photoelectron spectrometer (Physical Electronics) with an Al K alpha monochromatic X-ray source (1486.71 eV photon energy) was employed to collect XPS spectra. The pressure in the analysis chamber was maximum of 5×10^{-9} Torr during measurements. The chosen take-off angle and X-ray spot size were 45 degrees and 200 μm for high-resolution scans of Fe 2p, respectively. A pass energy of 23.5 eV and an energy step size of 0.1 eV were employed. Casa XPS software was used for fitting the acquired XPS data, using a Shirley background.

Ellipsometry measurements were conducted to measure the thickness of the passive layers of both samples. The passive layers were formed by potentiostatic polarization at 0.2 V (vs. Ag/AgCl) for 3 h in a 0.1 M NaOH solution. A visual variable angle spectroscopic ellipsometry (M2000X VIS-VASE) provided by J. A. Woollam Co., Inc. with Xenon lamp source was used for the measurements. WVASE software was employed to analyze the ellipsometry data.

3. Results & discussion

3.1. Analysis of microstructural features

High-resolution electron backscattered diffraction (EBSD) measurements were performed to determine the spatially resolved crystallographic orientations and consequently the defect density (grain boundary area fraction and dislocation density) through the local orientation distributions. The EBSD measurements were conducted in several longitudinal sections perpendicular to transverse direction (TD), rolling direction (RD) and normal direction (ND)) to trace possible differences in these various planes. The results on the ND-TD plane are only shown due to the plane of interest for the current study. Furthermore, the same step size for the EBSD measurements performed on LD and HD samples were employed to prevent the effect of step size on the calculation of boundaries and dislocation density [16].

Figs. 1a and b show the EBSD inverse pole figures (IPF) in ND-TD plane of the low defect (LD) and high defect (HD) samples, respectively. The LD microstructure consists of equiaxed grains while having a mild preferential orientation for <111> //ND, <100> //ND and <112> //ND, <113> //ND, <114> //ND planes which is a result of the β fiber texture of austenite to ferrite transformation [17]. However, a stronger preferential crystallographic orientation in <111> //ND and <100> //ND (Fig. 1b) and also components in <112> //ND, <113> //ND, <114> //ND planes is observed in HD material. In this case, the components mentioned above appeared as a result of the α and γ fiber rolling textures [18,19]. Therefore, the intensity (magnitude) and the exact components which are preferred are different. However, both samples have a similar distribution of preferential crystal orientations with respect to the crystal direction, which is parallel to ND. Furthermore, in Fig. 1a and b, the microstructure of both LD and HD samples belongs only in the BCC crystal structure. It shows that both materials consist of only the ferritic phase. Both materials do not exhibit carbides in IPF maps, showing the negligible volume fraction of carbides due to the very low alloyed nature of the material.

In Figs. 1c and d, the geometrically necessary dislocation (GND) maps of LD and HD samples are given, respectively. It is observed that dislocations in LD samples (Fig. 1c) are homogeneously distributed with
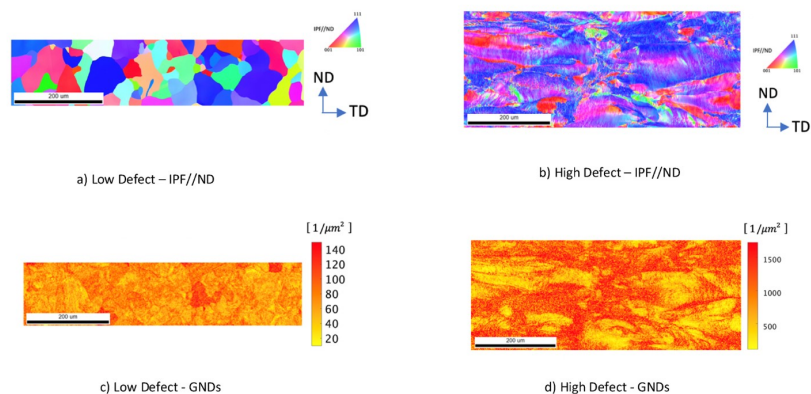

a) Low Defect − IPF//ND

b) High Defect − IPF//ND

c) Low Defect - GNDs

d) High Defect - GNDs

Fig. 1. EBSD maps of the hot- and cold- rolled samples. (a) and (b) are the Inverse Pole Figure (IPF) maps show the spatially resolved crystallographic orientations parallel to the normal direction of the sheets for the low- Defect (HD) and (b) the high- Defect (LD) samples, respectively. (c) and (d) are the Geometrically Necessary Dislocation (GND) maps (measured with the same step size of 0.5 μm) for LD and HD samples. The GNDs were calculated for a maximum angle of 10° and up to the 3rd neighbour pixel.

very low density. In Fig. 1d, it is shown that the HD exhibits a much higher dislocation density, consisting of topological heterogeneities (e.g. the largest GND density is observed at highly distorted regions while other regions do not contain large orientation gradients). The mean dislocation density values are $3.6 \pm 0.4 \times 10^{12} \, m^{-2}$ and $147 \pm 14 \times 10^{12}$ m^{-2} for the low defect (LD) and high defect (HD) samples, respectively. It shows that there are almost two orders of magnitude difference in dislocation density between both samples. Concerning the defect density, as it was previously mentioned, the quantification of the dislocation density refers to only the structural dislocations (GNDs) and not to statistically stored dislocation (SSD) density. Although SSDs can highly contribute to the material's dislocation content, the studied material is characterized by a high Stacking-Fault Energy (SFE), and in such metals, sub-cell structures would be expected to be prevalent [20–22]. This occurs due to the dislocations' cross-slip during deformation which results in the formation of favourable (lower) energy arrangements of the dislocation content (mechanism of dynamic recovery – a phenomenon known as polygonization [23,24]). Hence, in such metals the largest contribution of the dislocation density can be reasonably expected to be located at the substructure's boundaries.

Similar to geometrically necessary dislocation density, the grain boundary fraction is much higher in HD samples. Considering the threshold angle for high angle grain boundaries (HAGB) as $15°$, the HAGB for HD and LD samples are 0.152 ± 0.002 and $0.029 \pm 0.001 / \mu m$, respectively. HD samples also exhibit higher low-angle grain boundary density in comparison with LD samples. The LAGB density for HD samples is $2.44 \pm 0.14 / \mu m$, whereas the LAGB density for LD samples is $0.006 \pm 0.002 / \mu m$.

3.2. Reactivity of the surface – SKP experiments

To elucidate the effect of microstructural defects on the reactivity of the surface, SKP point measurements were conducted on freshly polished surfaces of both low (LD) and high defect (HD) density samples. Fig. 2a shows the work function changes over time at the measured points. On both samples, an initial increase in the work function is observed and associated with the evaporation of absorbed water layer on the surface and the growth of natural passive layer [25]. The further increase in the work function probably results from the further growth of a natural passive layer. In Fig. 2b, the work function values at three selected exposure times after reaching the stability are given. It is observed that the work function is lower for HD samples than for LD samples at all times. The decrease in work function with increasing

defect density agrees with the existing literature that report decreases in work function with an increase in microstructural defect density, introduced by plastic deformation on steel samples [10,26,27]. The work function is defined as the minimum necessary work to take an electron from the sample to a point outside of sample where its contribution from image forces are eliminated [28]. Therefore, the HD samples that have lower work function are more electrochemically reactive.

3.3. Passive layer analysis

Chemical composition - X-ray photoelectron spectroscopy (XPS) measurements were conducted to investigate the chemical composition of the passive layers. High-resolution Fe $2p_{3/2}$ photoelectron spectra between 704 and 717 eV of both high defect (HD) and low defect (LD) samples are given in Fig. 3. Multiplet-split fitting was applied for fitting the Fe $2p_{3/2}$ photoelectron spectra since multiplet splitting occurs due to unpaired D-orbital electrons in high-spin Fe^{+2} and Fe^{+3} species [29]. The reported optimized fitting parameters by Biesinger et al. [30] were used for the fitting of data and represented as single peaks for $Fe°$, Fe^{+2} and Fe^{+3} after background subtraction. From the fitting analysis of the Fe $2p_{3/2}$, composition of the passive layer consists of Fe_3O_4, γ-Fe_2O_3 and FeO(OH). Based on previous studies [31–35], we assumed that the passive layer consists of a bi-layered oxide layer (Fe_3O_4 and γ-Fe_2O_3) and an outer FeO(OH) layer. The differences in peak intensities show that the fractions of the oxides differ between HD and LD samples. The phase fractions are calculated according to fitting parameters and given in Table 2. The lower ratio of Fe^{+3}/Fe^{+2} peak intensity in HD samples indicates that the fraction of γ-Fe_2O_3 in the passive layer is lower for HD samples. The γ-Fe_2O_3 percent on HD samples is approximately a 66 % of the total passive layer versus the 75 % observed on the LD samples.

Passive layer thickness – Ellipsometry measurements were conducted after potentiostatic passivation of the samples. The following optical constants of 3.180–3.850 i for the iron substrate and 2.550–0.350 i for the thin iron oxide film (Fe_3O_4 and γ-Fe_2O_3) were used into the model to estimate the oxide thickness [36]. The thicknesses of the passive layers formed on HD and LD samples are 2.54 ± 0.11 and 1.67 ± 0.07 nm, respectively. From SKP results, the elucidated high-reactivity of the HD samples can explain a faster kinetic of the passive layer growth resulting in a thicker passive layer.

3.4. Electrochemical characterization

Potentiodynamic polarization (PDP) – Potentiodynamic polarizations

a)   b)
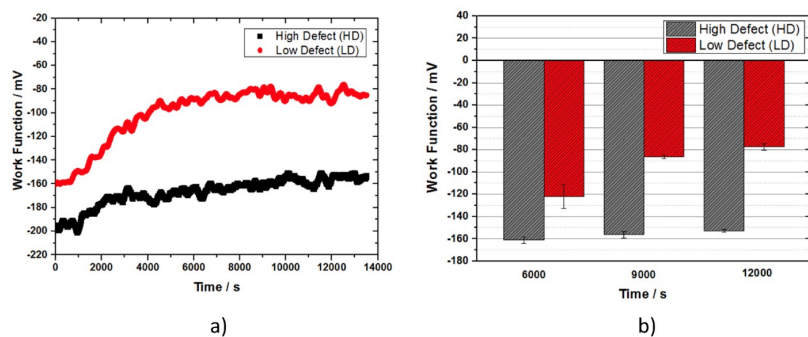
Fig. 2. a) SKP point measurements on fresh polished samples with 550 µm stainless steel probe, at ambient temperature and 43 % RH as a function of time b) Work function values measured at selected exposure times.
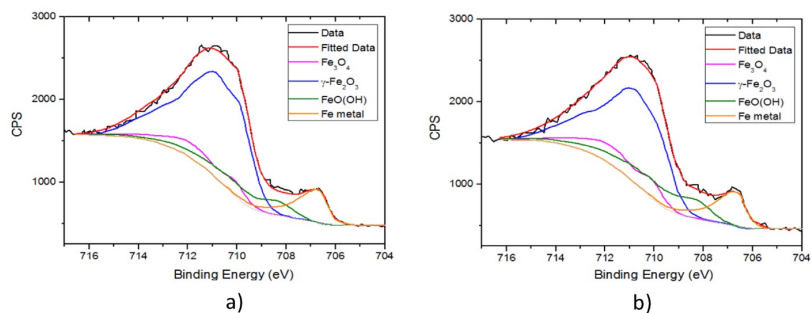
Fig. 3. Experimental Fe 2p spectrum from the XPS measurement and corresponding fitting of the spectrum for the passivated a) LD and b) HD samples. Passive layer formed after potentiostatic polarization for 3 h at 0.2 V (vs. Ag/AgCl) in 0.1 M NaOH solution.

Table 2
Oxide fractions of the passive layers calculated from the fitting XPS Fe 2p spectrum.

	γ-Fe$_2$O$_3$(%)	Fe$_3$O$_4$(%)	FeO(OH)(%)
Low Defect (LD)	74.8	13.4	11.8
High Defect (HD)	65.9	18.8	15.3

were conducted in a 0.1 M NaOH solution, which ensures the formation of a passive layer due to alkaline environment. In Fig. 4a, potentiodynamic polarization curves obtained from both HD and LD samples are given. Both samples show similar curves with the main difference in the passivity current densities. It is observed that current density values are higher for HD samples comparison to LD samples. Fig. 4b shows the values at the potentials of 0, 0.25 and 0.5 V (vs. Ag/AgCl) for both samples. For all the potentials, the current density values are approximately 1.5 times higher in HD samples than in LD samples, indicating higher electronic and/or ionic conductivity of the passive film in HD samples.

Potentiostatic polarization – Fig. 5a shows the current density transients of both samples during potentiostatic polarization at 0.2 V (vs. Ag/AgCl) in 0.1 M NaOH solution. The initial current density values are associated with the charging of the double layer on both samples [37]. The sharp decrease in current density values on both samples in the first few seconds of measurements stems from the initial formation of the insulating passive layer. The further decline in current density values is due to the growth of the passive film. After 3 h of polarization, the current density transients of both samples approach to steady-state, at which the rates of formation and dissolution of the passive film are equal to each other. Fig. 5b shows the current density values measured after 3 h of polarization. It is observed that the current density of values HD samples is more than 1.5-fold higher than the one of LD samples. This suggests that the conductivity of passive film HD samples are higher than the passive film formed on LD samples, in agreement with the current density trends observed in the passive region of potentiodynamic polarization curves.

Electrochemical Impedance Spectroscopy (EIS) – EIS data were collected after passivating both samples. The Nyquist plots of both samples (Fig. 6a) show that a larger arc is produced in LD samples in comparison to HD samples. It indicates the lower barrier properties of the passive layer formed on HD samples, in agreement with the current-
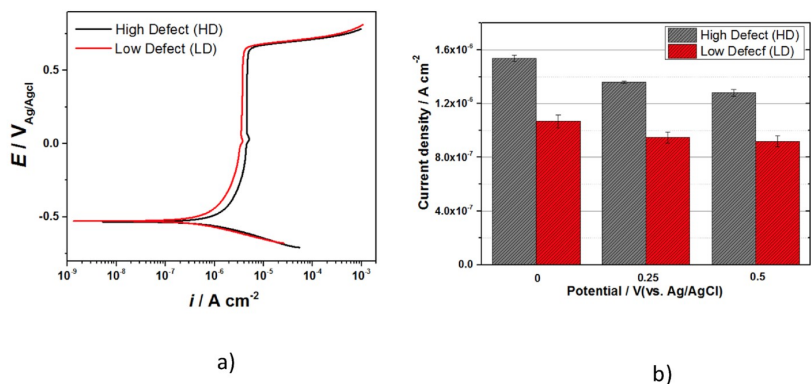

Fig. 4. a) Potentiodynamic polarization curves of LD and HD samples in 0.1 M NaOH solution b) Current density values from PD curves at the potentials 0, 0.25 and 0.5 V (vs. Ag/AgCl).
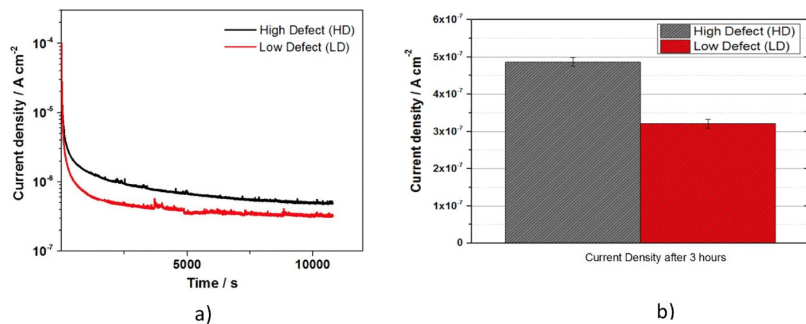
Fig. 5. a) Current vs time curves during potentiostatic polarization at 0.2 V (vs. Ag/AgCl) in 0.1 M NaOH solution b) Current density values of samples after 3 h of potentiostatic polarization.
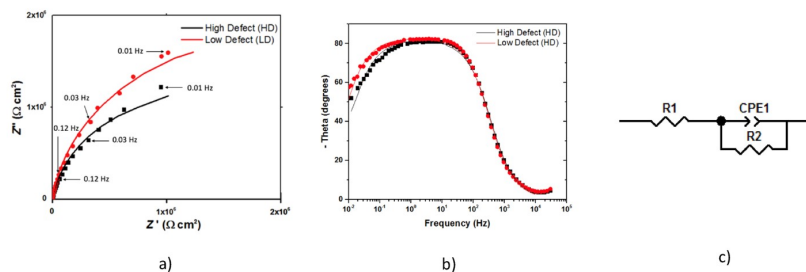

Fig. 6. a) Nyquist and b) Phase angle plots of LD and HD samples collected after passivation with potentiostatic polarization at 0.2 V (vs. Ag/AgCl) for 3 h in 0.1 M NaOH solution c) Equivalent electrical circuit (EEC) used to interpret the EIS data for HD and LD samples. Solid lines show the fitted curves by the proposed equivalent circuit.

density values observed in the passive region of the potentiodynamic polarization curves. In Fig. 6b, the phase angle plots of both samples are given. It is shown that EIS data exhibit a single time constant in both samples.

The equivalent electrical circuit (EEC) fitting of EIS data was conducted with the circuit shown in Fig. 6c with a constant phase element (CPE) instead of a pure capacitor in line with the literature [11,37–39]. The deviation from the ideal capacitive behaviour can be associated with the inhomogeneities in the passive film [40,32]. In the EEC, R_1 is attributed to the resistivity of the solution. R_2 and CPE_2 are related to resistive and capacitive behaviour of the passive film, respectively. The values obtained from the fitting are given in Table 3. The resistance values of passive layer R_2 are higher for LD samples in comparison to HD

Table 3
Equivalent circuit parameters obtained by fitting the collected EIS data of LD and HD samples. Parameters are the averaged values and standard deviation resulting from three measurement repetitions.

	R_1 (Ω cm^2)	R_2 Ω cm^2) x10^6	CPE$_1$-Q (Ω^{-1} s^n cm^2 x10^{-6})	CPE$_1$-n	C_1 (μF/ cm^2)
Low Defect (LD)	184 ± 10	3.55 ± 0.04	5.17 ± 0.04	0.91 ± 0.01	6.90 ± 0.07
High Defect (HD)	176 ± 10	2.77 ± 0.01	4.57 ± 0.01	0.91 ± 0.01	5.83 ± 0.01

samples.

The capacitance values were calculated using the Hsu and Mansfeld [41] formula in Eqn. 1 [41]:

$$C = R^{\frac{(1-n)}{n}} Q^{\frac{1}{n}} \qquad (1)$$

The calculated values (C_1) are presented in Table 3. From them, the thickness of the passive film can be estimated from Eqn 2 [42].

$$d_f = \frac{\varepsilon \varepsilon_o}{C_f} \qquad (2)$$

where d_f is the passive layer thickness, C_f is the capacitance value of the passive film, $\varepsilon = 40$ [43,44] and ε_o are the dielectric constant of passive film on low carbon steel and permittivity in vacuum, respectively. The thickness obtained from the capacitance values is 2.21 ± 0.01 nm and 1.87 ± 0.01 nm for HD and LD samples, respectively. These values are in reasonable agreement with the values obtained from ellipsometry measurements.

Capacitance measurements – Mott-Schottky (M–S) analysis was applied to characterize the semi-conductive properties of passive films. From M–S analysis, it is possible to quantify the defect density in an oxide film.

The total capacitance of the passive film is generally considered as the combination of two capacitors in series, representing the space charge capacitance region and the Helmholtz layer. The contribution of

the Helmholtz layer on the capacitance of the passive layer (much larger than the space charge layer) is negligible due to the strong presence of the passive layer. Thus, the capacitance of passive film can be considered as the capacitor of the space charge layer. Therefore, the Mott-Schottky relationship (Eqn. 3) can be applied to quantify the number of defects in the passive layer:

$$\frac{1}{C^2} = 2(E - E_{FB} - kT/q) / \varepsilon\varepsilon_o q\, N_d \quad\quad (3)$$

where T is the temperature, k the Boltzmann constant, E_{FB} the flat band potential, N_d the donor density, q the electron charge, ε_0 the permittivity of vacuum and $\varepsilon = 40$ [43] the dielectric constant of the iron oxide films formed on carbon steels. Experiments were carried out at the frequency of 1 kHz. At this value, the capacitance of iron oxide is not significantly affected by the applied frequency, and the electronic part of the space charge capacitance can be evaluated [45].

Fig. 7 shows the Mott-Schottky plots obtained after forming the passive layer at 0.2 V (vs. Ag/AgCl) for 3 h. The positive slope in the Mott-Schottky plots illustrates n-type semi-conductor behaviour of the passive layer [43,46]. This slope is inversely proportional to the donor density, the higher slope meaning a lower donor density. The deviation from linearity above 0 V (vs. Ag/AgCl) can be associated with the changes in passive film structure/composition [47]. The donor density values calculated from the linear slopes in the Mott-Schottky plots are given in Table 4. The donor density values are in the same order of magnitude with the previously reported for low carbon steels [48] and pure iron [38,49]. It is shown that the donor density values are approximately 1.5 times higher in HD samples than in LD ones, showing that the donor density increases with an increase in the defect density. The donor population in the passive film mainly consists of oxygen vacancies and cation interstitials [50]. The lower donor density in LD samples that have a lower defect density indicates the decrease of the concentration of Fe^{+2} in the passive layer due to the oxidation of Fe^{+2} to Fe^{+3} [45]. Furthermore, the differences in flat band potential also indicate differences in the fractions of Fe_3O_4, γ-Fe_2O_3 and FeO(OH) in passive films. These are in line with a higher concentration of Fe^{+2} in passive layers as measured with XPS when the defect density increased.

To understand the role of defect density on passive layer properties, it is required to prevent the combined effect of other microstructural features with defect density. The very low alloyed nature of the interstitial-free ferritic steels allows preventing the effect of chemical composition that might lead to alloying element segregation after cold rolling. Furthermore, the low alloying content also excludes the

Table 4
Donor density and Flat band potential values obtained from Mott-Schottky analysis.

	Donor Density N_d (10^{20} cm^{-3})	Flat Band Potential (vs Ag/AgCl)/V
Low Defect (LD)	4.6 ± 0.1	-0.73 ± 0.03
High Defect (HD)	6.8 ± 0.4	-0.79 ± 0.02

formation of inclusions and different phases. In this way, these microstructural features do not play a role in the passive layer properties and only the microstructural defect density is the main influencing feature. Crystallographic orientation is also a feature that may influence the formation of the passive layer. The EBSD measurements reveal the formation of stronger preferential orientation in <111 > //ND and <100 > //ND in HD samples than in LD samples. However, in our other research on the effect of cold rolling in the corrosion behaviour of IF steels, it is demonstrated that the dislocation density is still the dominant feature versus the effect of the crystallographic orientation [51]. In conclusion, no other microstructural features are influencing significantly the passive layer properties than the difference in microstructural defect densities between the samples, HD and LD. The microstructural defects relate to geometrically necessary dislocation (GND) density and grain boundary density.

SKP measurements demonstrate that the sample with higher defect density (HD sample) shows more negative surface potential and a faster kinetic to achieve stability of the potential. It indicates that the significant difference of microstructural defect densities leads to higher reactivity of the surface. These results explain the formation of thicker passive films in the HD sample measured by ellipsometry experiments. Polarization and EIS measurements show that the barrier properties of passive film worsen with the increase in microstructural defect density in the IF steel substrate. The passive layer consists of the oxides, Fe_3O_4 and γ-Fe_2O_3 and the presence of FeO(OH). The protective properties of the passive layer are mainly attributed to the presence of γ-Fe_2O_3. The band gap of Fe_3O_4 is 0.1 eV [52] whereas the band gap of γ-Fe_2O_3 is 2.3 eV [53]. Since the lower band gap leads to easing in electron transfer, Fe_3O_4 has significantly higher conductivity. Moreover, FeO(OH) layer has a less dense and more porous structure than γ-Fe_2O_3 [54,55]. Hence, it is considered that Fe_3O_4 and FeO(OH) layer do not have significant contribution in the protection properties of the passive film. XPS analysis shows slightly lower fraction of γ-Fe_2O_3 in the passive film of the sample with higher microstructural defect density (HD sample). However, this result cannot solely explain the difference on the resistances of the passive films from EIS analysis, with a decrease of approximately 20 % on the value of the resistance for the HD sample when compared to the LD sample. Taking also into consideration that the sample with higher defect density forms a thicker passive film that usually is associated with better protective properties.

The capacitance measurements and Mott-Schottky analysis uncover differences in the donor density in the passive films. The donor density in the passive films increases with the increasing of microstructural defect density. This increase probably stems from the fact that the increase in microstructural defect density leads to higher density of active sites, i.e. kinks, jogs, inducing the formation of a defective passive layer at these active sites [11]. In terms of the electronic conductivity, the increase in donor density leads to a smaller band gap in metal oxides [56,57], increasing the electronic conductivity by easing electron transfer. From the ionic conductivity point of view, the donors in the passive film carry ionic charges in iron oxides [58,59], and therefore the higher donor density leads to larger ionic conductivity.

Yamamoto et al. [11] showed that most of the donors in the passive film of pure iron are oxygen vacancies instead of cation interstitials in highly deformed samples. Since the formation of passive film and the semi-conductive properties of passive film are governed by the reaction
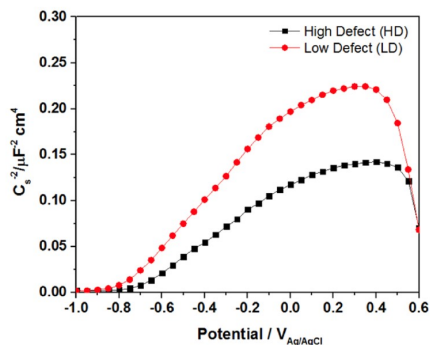

Fig. 7. Mott-Schottky plot of samples collected after forming passive layer at 0.2 V (vs. Ag/AgCl) for.3 h.

inducing the formation of oxygen vacancies, a thicker passive layer with higher donor density occurs in HD samples. On the side of LD samples, the existing donors arise due to incomplete film aging [11] since the very low density of substrate's microstructural defect density has a minimal effect on the formation of donors in passive film, as opposed to HD samples. Ageing the film further in time, potentiostatic polarization would result in a passive film with a lower donor density and better passive layer properties.

These results demonstrate that the microstructural defects, dislocation density and grain boundary area, influence the properties of the passive layer. Nevertheless, further investigation is necessary to differentiate and quantify the influence of the single features.

4. Conclusions

In this work, the role of microstructural defect density on the passive layer properties formed on IF steels are investigated in a 0.1 M NaOH solution. The sample with higher defect density presents higher reactivity indicated by the more negative work function. This results in the formation of a thicker passive layer when compared to the specimen with lower defect density. XPS measurements on passive layers formed by potentiostatic polarization, show that the passive layer consists of Fe_3O_4, γ-Fe_2O_3 and FeO(OH), regardless of the defect density. However, the volume fraction of γ-Fe_2O_3 passive film slightly decreases with increasing defect density. Moreover, Mott-Schottky analysis shows that the higher substrate defect density leads to a higher donor density of passive film. Electrochemical results from potentiodynamic polarization and EIS experiments indicate that the passive film of the higher defective sample has worse barrier properties. This is attributed to the decrease in the volume fraction of γ-Fe_2O_3 and the increase in donor density of passive film. In conclusion, the presence of higher microstructural defect density on the IF steel substrate enhances the growth of thicker but highly defective passive layers.

Data availability

The raw/processed data required to reproduce these findings can be shared upon request.

CRediT authorship contribution statement

A. Yilmaz: Conceptualization, Investigation, Methodology, Validation, Data curation, Writing - original draft, Writing - review & editing, Visualization. **K. Traka:** Methodology, Investigation, Validation, Data curation, Writing - original draft, Writing - review & editing, Visualization. **S. Pletincx:** Methodology, Investigation, Validation, Data curation, Writing - review & editing, Visualization. **T. Hauffman:** Methodology, Validation, Writing - review & editing, Supervision. **J. Sietsma:** Methodology, Conceptualization, Validation, Writing - review & editing, Supervision, Project administration. **Y. Gonzalez-Garcia:** Methodology, Conceptualization, Validation, Writing - review & editing, Supervision, Project administration.

Declaration of Competing Interest

The authors declare no conflict of interest.

Acknowledgements

Appendix A. Supplementary data

Supplementary material related to this article can be found, in the online version, at doi:https://doi.org/10.1016/j.corsci.2021.109271.

References

[1] A. D.R, Strain Hardening and Annealing, The Science and Engineering of Materials, Boston, MA, 1996.
[2] S. Zaefferer, J. Ohlert, W. Bleck, A study of microstructure, transformation mechanisms and correlation between microstructure and mechanical properties of a low alloyed TRIP steel, Acta. Mater. 52 (9) (2004) 2765–2778.
[3] K.L. Murty, M.D. Mathew, Y. Wang, V.N. Shah, F.M. Haggag, Nondestructive determination of tensile properties and fracture toughness of cold worked A36 steel, Int. J. Press. Vessel. Pip. 75 (11) (1998) 831–840.
[4] J.P. Chu, J.M. Rigsbee, G. Banaś, H.E. Elsayed-Ali, Laser-shock processing effects on surface microstructure and mechanical properties of low carbon steel, Mater. Sci. Eng. A 260 (1–2) (1999) 260–268.
[5] W. Karlsen, S. Van Dyck, The effect of prior cold-work on the deformation behaviour of neutron irradiated AISI 304 austenitic stainless steel, J. Nucl. Mater. 406 (1) (2010) 127–137.
[6] S. Takahashi, J. Echigoya, T. Ueda, X. Li, H. Hatafuku, Martensitic transformation due to plastic deformation and magnetic properties in SUS 304 stainless steel, J. Mater. Process. Technol. 108 (2) (2001) 213–216.
[7] M. Takahashi, H.K.D.H. Bhadeshia, Model for transition from upper to lower bainite, Mater. Sci. Technol. 6 (7) (1990) 592–603.
[8] Jinlong Lv, L. Hongyun, Electrochemical investigation of passive film in pre-deformation AISI 304 stainless steels, Appl. Surf. Sci. 263 (2012) 29–37, no. 0.
[9] J. Lv, H. Luo, Effects of strain and strain-induced α′-martensite on passive films in AISI 304 austenitic stainless steel, Mater. Sci. Eng. C 34 (1) (2014).
[10] J. Lv, W. Guo, T. Liang, The effect of pre-deformation on corrosion resistance of the passive film formed on 2205 duplex stainless steel, J. Alloys. Compd. 686 (2016) 176–183.
[11] T. Yamamoto, K. Fushimi, S. Miura, H. Konno, Influence of substrate dislocation on passivation of pure Iron in pH 8. 4 borate buffer solution, J. Electrochem. Soc. 157 (7) (2010) 231–237.
[12] X.Y. Wang, D.Y. Li, Mechanical and electrochemical behavior of nanocrystalline surface of 304 stainless steel, Electrochim. Acta 47 (24) (2002) 3939–3947.
[13] B.L. Adams, J. Kacher, EBSD-based microscopy: resolution of dislocation density, Comput. Mater. Contin. 14 (3) (2009) 183–194.
[14] F. Nye, Some geometrical relations in dislocated crystals, Acta Metall. 1 (1953) 153–162.
[15] F. Bachmann, R. Hielscher, H. Schaeben, Texture analysis with MTEX- Free and open source software toolbox, Solid State Phenom. 160 (2010) 63–68.
[16] J. Jiang, T.B. Britton, A.J. Wilkinson, Measurement of geometrically necessary dislocation density with high resolution electron backscatter diffraction: effects of detector binning and step size, Ultramicroscopy 125 (2013) 1–9.
[17] L.A.I. Kestens, H. Pirgazi, Texture formation in metal alloys with cubic crystal structures, Mater. Sci. Technol. (United Kingdom) 32 (13) (2016) 1303–1315.
[18] B.B. Hutchinson, Deformation Microstructures and textures in steels, Philos. Trans. R. Soc. Lond. Ser. Math. Phys. Eng. Sci 357 (1999) 1471–1485.
[19] R.K. Ray, J.J. Jonas, R.E. Hook, Cold rolling and annealing textures in low carbon and extra low carbon steels, Int. Mater. Rev. 39 (January 4) (1994) 129–172.
[20] Y. Inokuti, R.D. Doherty, Transmission kossel study of the structure of compressed iron and its recrystallization behaviour, Acta Metall. 26 (1) (1978) 61–80.
[21] B. Hutchinson, Deformation microstructures and textures in steels, Philos. Trans. R. Soc. Lond. Ser. Math. Phys. Eng. Sci 357 (1756) (1999).
[22] B. Hutchinson, Nucleation of recrystallisation, Scr. Met. Mater. 27 (11) (1992) 1471–1475.
[23] R.W. Cahn, Recrystallization of single crystals after plastic bending, J. Inst. Met. 76 (2) (1949) 121.
[24] R.W. Cahn, Internal strains and recrystallization, Prog. Met. Phys. 2 (1950) 151–176.
[25] Ö. Özkanat, B. Salgin, M. Rohwerder, J.M.C. Mol, H. De Wit, H. Terryn, Scanning Kelvin probe study of (Oxyhydr)oxide surface of aluminum alloy, J. Phys. Chem. C 116 (2) (2012) 1805–1811.
[26] W. Li, M. Cai, Y. Wang, S. Yu, Influences of tensile strain and strain rate on the electron work function of metals and alloys, Scr. Mater. 54 (5) (2006) 921–924.
[27] A. Nazarov, D. Thierry, Application of Volta potential mapping to determine metal surface defects, Electrochim. Acta. 52 (27) (2007) 7689–7696. SPEC. ISS.
[28] M. Rohwerder, F. Turcu, High-resolution Kelvin probe microscopy in corrosion science: scanning Kelvin probe force microscopy (SKPFM) versus classical scanning Kelvin probe (SKP), Electrochim. Acta. 53 (2) (2007) 290–299.
[29] R.P. Gupta, S.K. Sen, Calculation of multiplet structure of core p-vacancy levels, Phys. Rev. B 10 (1) (1974) 71–77.
[30] M.C. Biesinger, B.P. Payne, A.P. Grosvenor, L.W.M. Lau, A.R. Gerson, R.S.C. Smart, Resolving surface chemical states in XPS analysis of first row transition metals, oxides and hydroxides: Cr, Mn, Fe, Co and Ni, Appl. Surf. Sci. 257 (7) (2011) 2717–2730.
[31] M.P. Strehblow H, X-ray photoelectron spectroscopy in corrosion research, in: P. Marcus, F. Mansfeld (Eds.), Analytical Methods in Corrosion Science and Engineering, CRC Press Taylor Fr., 2006.

[32] L. Freire, X.R. Nóvoa, M.F. Montemor, M.J. Carmezim, Study of passive films formed on mild steel in alkaline media by the application of anodic potentials, Mater. Chem. Phys. 114 (2–3) (2009) 962–972.

[33] I.V. Sieber, H. Hildebrand, S. Virtanen, P. Schmuki, Investigations on the passivity of iron in borate and phosphate buffers, pH 8.4, Corros. Sci. 48 (11) (2006) 3472–3488.

[34] Y. Li, Y.F. Cheng, Passive film growth on carbon steel and its nanoscale features at various passivating potentials, Appl. Surf. Sci. 396 (2017) 144–153.

[35] H.H. Strehblow, Passivity of metals studied by surface analytical methods, a review, Electrochim. Acta 212 (2016) 630–648.

[36] G. O, N.S.K. Kudo, T. Shibata, Ellipsometric and radiotracer measurements of the passive oxide film on fe in neutral solution, Corros. Sci. 8 (1968) 809–814.

[37] K. Yanagisawa, T. Nakanishi, Y. Hasegawa, K. Fushimi, Passivity of dual-phase carbon steel with ferrite and martensite phases in pH 8.4 boric acid-borate buffer solution, J. Electrochem. Soc. 162 (7) (2015) C322–C326.

[38] Y. Takabatake, K. Fushimi, T. Nakanishi, Y. Hasegawa, Grain-dependent passivation of Iron in sulfuric acid solution, J. Electrochem. Soc. 161 (14) (2014) C594–C600.

[39] K. Fushimi, Y. Takabatake, T. Nakanishi, Y. Hasegawa, Microelectrode techniques for corrosion research of iron, Electrochim. Acta 113 (2013) 741–747.

[40] M. Büchler, P. Schmuki, H. Böhni, Iron passivity in borate buffer: formation of a deposit layer and its influence on the semiconducting properties, J. Electrochem. Soc. 145 (2) (1998) 609–614.

[41] C.H. Hsu, F. Mansfeld, Concernng the conversion of the constant phase element parameter Y0 into a capacitance, Corrosion 57 (9) (2001) 747–748.

[42] A.J. Bard, L.R. Faulkner, Electrochemical Methods: Fundamentals and Applications, 2nd. ed., John Wiley & Sons, 2001.

[43] K. Azumi, Mott-schottky plot of the passive film formed on Iron in neutral borate and phosphate solutions, J. Electrochem. Soc. 134 (6) (1987) 1352.

[44] K. Azumi, T. Ohtsuka, N. Sato, Impedance of Iron electrode passivated in borate and phosphate solutions, Trans. Jpn. Inst. Met. 27 (5) (1986) 382–392.

[45] S.J. Ahn, H.S. Kwon, Effects of solution temperature on electronic properties of passive film formed on Fe in pH 8.5 borate buffer solution, Electrochim. Acta 49 (20) (2004) 3347–3353.

[46] J.H. Kennedy, K.W. Frese, Flatband potentials and donor densities of polycrystalline α -Fe2O3 determined from mott-schottky plots, J. Electrochem. Soc. 125 (5) (1978) 723–726.

[47] E.M.A. Martini, I.L. Muller, Characterization of the film formed on iron borate solution by electrochemical impedance spectroscopy, Corros. Sci. 42 (3) (2000) 443–454.

[48] M. Sánchez, J. Gregori, C. Alonso, J.J. García-Jareño, H. Takenouti, F. Vicente, Electrochemical impedance spectroscopy for studying passive layers on steel rebars immersed in alkaline solutions simulating concrete pores, Electrochim. Acta. 52 (27) (2007) 7634–7641. SPEC. ISS.

[49] S.P. Harrington, F. Wang, T.M. Devine, The structure and electronic properties of passive and prepassive films of iron in borate buffer, Electrochim. Acta 55 (13) (2010) 4092–4102.

[50] J. Liu, D.D. Macdonald, The passivity of Iron in the presence of ethylenediaminetetraacetic acid. II. The defect and electronic structures of the barrier layer, J. Electrochem. Soc. 148 (11) (2001) B425.

[51] A. Yilmaz, C. Örnek, K. Traka, J. Sietsma, Y. Gonzalez-Garcia, "Combining surface Volta-potential with electrochemical measurements to investigate the role of cold working on corrosion behavior of interstitial free (IF) steels," To be Publ.

[52] R.M. Cornell, U. Schwertmann, The Iron Oxides; Structure Properties, Reactions, Occurrences and Uses, 2003.

[53] L. Hamadou, A. Kadri, N. Benbrahim, Characterisation of passive films formed on low carbon steel in borate buffer solution (pH 9.2) by electrochemical impedance spectroscopy, Appl. Surf. Sci. 252 (5) (2005) 1510–1519.

[54] W. Xu, K. Daub, X. Zhang, J.J. Noel, D.W. Shoesmith, J.C. Wren, Oxide formation and conversion on carbon steel in mildly basic solutions, Electrochim. Acta 54 (24) (2009) 5727–5738.

[55] F. Watari, P. Delavignette, J. Van Landuty, S. Amelinckx, Electron microscopic study of dehydration transformations. Part III: High resolution observation of the reaction process FeOOH → Fe2O3, J. Solid State Chem. 48 (1) (1983) 49–64.

[56] J. Wang, et al., Oxygen vacancy induced band-gap narrowing and enhanced visible light photocatalytic activity of ZnO, ACS Appl. Mater. Interfaces 4 (8) (2012) 4024–4030.

[57] S.A. Ansari, M.M. Khan, M.O. Ansari, S. Kalathil, J. Lee, M.H. Cho, Band gap engineering of CeO2 nanostructure using an electrochemically active biofilm for visible light applications, RSC Adv. 4 (32) (2014) 16782–16791.

[58] T. Sato, Norio ; Noda, Ion Migration in Anodic Barrier Oxide Films on Iron in Acidic Phosphate Solutions, Electrochim. Acta 22 (839–843) (1976).

[59] S.C. Hendy, N.J. Laycock, M.P. Ryan, Atomistic modeling of cation transport in the passive film on Iron and implications for models of growth kinetics, J. Electrochem. Soc. 152 (8) (2005) B271.